Phase shaping of dual-pumped Brillouin–Kerr frequency combs

Anastasiia Sheveleva, Moïse Deroh, Bertrand Kibler, Christophe Finot, Erwan Lucas

Phase-Shaping of Dual-Pumped Kerr Frequency Combs in Bichromatic Brillouin Lasers

Anastasiia Sheveleva*[1], Moise Deroh[1], Bertrand Kibler[1], Christophe Finot[1], and Erwan Lucas[1]

[1] *Laboratoire Interdisciplinaire Carnot de Bourgogne, UMR 6303 CNRS-Université de Bourgogne, 9 avenue Alain Savary, BP 47870, 21078 Dijon Cedex, France*

Compiled February 15, 2024

We investigate the spectral phase characteristics of dual-pumped Kerr frequency combs generated in a bichromatic Brillouin fiber laser architecture with normal dispersion, producing square-like pulse profiles. Using a pulse shaper, we measured the relative phase between the pump Stokes and adjacent lines, revealing a symmetric phase relationship. Our results highlight the absence of the abrupt phase difference typically observed with single continuous-wave pumping. By manipulating spectral amplitudes and phases, we demonstrate the transformation into various optical waveforms. The stability of our low-noise frequency comb ensures reliable performance in practical settings.

Optical frequency combs, characterized by their equally spaced and coherent spectral lines, have revolutionized various fields of optics and photonics, offering unprecedented precision in frequency metrology, spectroscopy [1]. Kerr frequency combs, generated through Kerr non-linearity in optical resonators [2], stand out for their potential in producing low-noise and highly stable frequency combs with high repetition rates, offering prospects in optical telecommunications. This paper explores the intricate dynamics of Kerr frequency combs, specifically focusing on the distinctive spectral phase features arising from dual pumping in a Brillouin laser configuration.

Advances in microresonator-based frequency comb generation have revealed a diverse array of comb patterns, ranging from dissipative solitons [3] to Turing rolls [4] and dark pulses [5]. Despite these developments, comprehensive understanding, characterizing, and manipulating [6, 7] the spectral and temporal features of these waveforms poses a significant challenge. Various experimental methods have been devised to characterize the spectral phase of the comb teeth. A common strategy involves equalizing the phase of the microcomb with a pulse shaper until a transform-limited pulse is inferred from an intensity autocorrelation measurement [8]. Other techniques leverage dual-comb interferometry [9–11] or cross-correlation [12] with a reference pulse . Additionally, for QCL-based combs, the shifted wave interference Fourier transform spectroscopy (SWIFT) method [13] employs beatnote demodulation measured through an interferometer to retrieve the phase difference between adjacent lines. A similar approach, adapted to heterodyne measurements and known as stepped heterodyne [14, 15], has been used for differential phase measurements.

This work presents a detailed investigation into the generation and control of Kerr frequency combs in a dual-pumped Brillouin laser setup [16, 17]. Our cavity relies on a highly nonlinear fiber (HNLF) with normal dispersion to trigger the formation of dark pulses, also known as switching waves [18]. Unlike the single continuous-wave (CW) pump scenario, where the phase of the pump line exhibits a discrete jump [5, 19], our dual-pumping configuration results in a smooth relative phase accumulation from line to line. This difference is a key aspect of our approach, and our study focuses on assessing the phase of the few center comb lines. To validate the robustness of our approach, we compare the experimental results with numerical simulations. The stability of the pulse trains and phase shaping is rigorously confirmed, setting the stage for the exploration of various arbitrary waveform generation.

Our comb generation method is adapted from [16]. The setup, shown in fig. 1, employs a Brillouin laser configuration with a fiber cavity closed by an optical circulator, eliminating clockwise resonance conditions. The cavity is mainly composed of a 10 m segment of HNLF, to enhance Brillouin and Kerr nonlinearities, and chosen to maintain normal net group velocity dispersion (GVD). Bichromatic pumping is achieved by using an electro-optic Mach-Zehnder modulator, creating tunable-spaced pumps (∼40 GHz) and a programmable filter to select the sidebands. Counterclockwise Brillouin Stokes gains, downshifted from the pumps by the phonon frequency, lead to dual Brillouin lasing and subsequent Kerr comb generation through cascaded four-wave mixing. To mitigate thermal drift, a phase lock loop stabilizes the frequency offset between one pump and its Stokes laser [20]. The bandwidth and symmetry of the comb are finely controlled by adjusting the offset frequency and the frequency spacing between the pumps [21]. This meticulous setup ensures stable and controlled comb generation, forming the basis for subsequent spectral shaping and phase retrieval investigations. The comb exiting the cavity is amplified before filtering and phase shaping in a programmable pulse-shaper (WaveShaper 4000S by Coherent/Finisar) [22, 23]. The shaped temporal waveforms are characterized on an optical sampling

*anastasiia.sheveleva@u-bourgogne.fr

oscilloscope (OSO) with sub-picosecond resolution and their optical spectrum on a high-resolution optical spectrum analyzer (OSA).

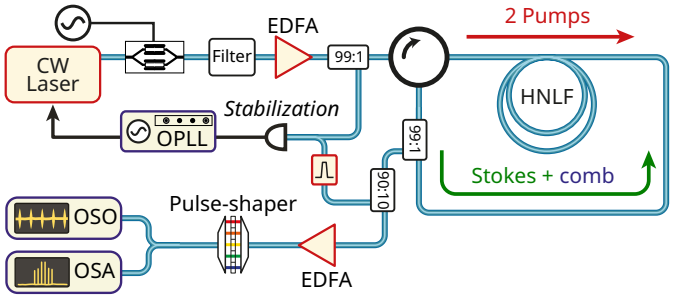

Fig. 1. Schematic of the experimental setup, involving a continuous-wave (CW) laser, erbium-doped fiber amplifiers (EDFA), a highly nonlinear fiber (HNLF), an optical phase-lock loop, an optical spectrum analyzer (OSA), and an optical sampling oscilloscope (OSO).

Figure 2a shows the measured optical spectrum at the cavity output (without filtering applied), which serves as a reference for our investigation. To provide a comprehensive understanding of the observed dynamics, we have developed a numerical simulation model based on coupled equations derived from the Ikeda map, combining the Brillouin coupled mode equations and the nonlinear Schrödinger equation (NLSE), as outlined in [16]. The iterative calculation of the nonlinear dynamics in the cavity involves two steps. First, the steady-state Brillouin intensity distribution is computed. Then, the modified NLSE, which includes the distributed Brillouin gain, is solved for each round trip using the split-step method. Remarkably, our simulation precisely reproduces the experimental spectrum (see fig. 2a), showcasing its robust capability to capture the intricate details of Kerr frequency comb generation within the bichromatic Brillouin laser setup. The slight asymmetry of the comb arises from an estimated ∼1.6 MHz mismatch between the frequency spacing of the injected pumps (39.9835 GHz) and an exact multiple of the 18.4 MHz cavity free spectral range (FSR) [21].

The numerical simulation allows us to further investigate the dynamics of the cavity, providing a detailed characterization of the spectral phase, that is, the relative dephasing between the comb lines and the pumps, as shown in fig. 2b. The simulated spectral phase reveals a distinctive behavior in which the comb lines do not exhibit the in-phase characteristics of a transform-limited pulse. Instead, the phase accumulates linearly and symmetrically from the pumps, similar to observations in microresonators under normal dispersion conditions [5]. In particular, in contrast to the continuous-wave (CW) driving case studied in previous work, our dual-pumping configuration displays a smooth phase accumulation of −0.96 radian per comb line, as illustrated in the inset of fig. 2b. Interestingly, the slight asymmetry in the comb lines' power also reflects in their phase, as we observe a minute imbalance of 0.15 rad between the lines adjacent to the Stokes lines. The non-parabolic phase profile suggests a nonuniform chirping of the pulse, a characteristic corroborated by the temporal intensity profile and the instantaneous phase, as shown in fig. 2c. The waveform adheres to the periodicity determined by the frequency spacing of the two Stokes waves, displaying a square-like pulse pattern characteristic of switching waves [18]. It has a full width at half-maximum (FWHM) duration of 10 ps, corresponding to a duty cycle of 0.4. The temporal profile reveals a pronounced chirp at the pulse edges, consistent with findings in ref. [5], and exhibits a phase jump at the intensity zero crossing.

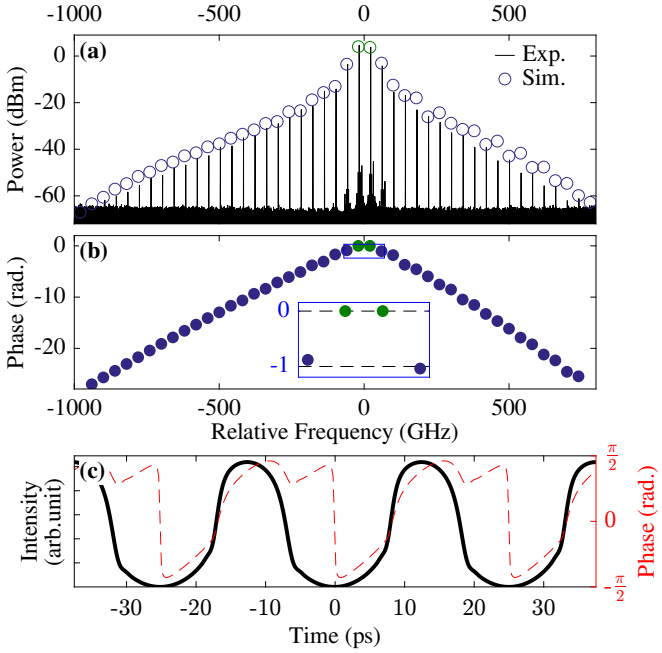

Fig. 2. Simulation results. **(a)** Measured comb out of cavity and simulated comb overlaid. The Stokes lines are marked in green. The total pump power is 280 mW. **(b)** Simulated spectral phases of the comb teeth shown in (a). **(c)** Simulated corresponding intracavity waveform with instantaneous phase.

Accurate spectral phase measurements in Kerr combs are challenging because of their complex waveforms, low pulse energy, and high repetition rates. In this study, we employed a common method involving a pulse-shaper to compensate the microcomb's spectral phase and retrieve a transform-limited pulse for analysis. Although previous investigations explored the phase profile of dark pulses under continuous-wave (CW) driving in a microresonator, confirming the profile depicted in fig. 2b [5], our approach involves a dual pump configuration. Our focus here lies on measuring the relative phase between the pump Stokes and the adjacent lines, aiming to validate the absence of abrupt phase differences.

To highlight this characteristic, we chose to retrieve the phase by analyzing temporal intensity profiles, deviating from the conventional autocorrelation approach. The spectrum is deliberately limited to four lines for simplicity, and we assume a symmetric spectrum in both amplitude and phase. These assumptions allow us to derive an analytical expression for the intensity, following the guidelines outlined in [24]. Taking into account the phase difference ϕ and the ratio between spectral amplitudes A of the Stokes and the adjacent lines, the profile is defined by

$$\boldsymbol{I}(\boldsymbol{t}) = 2\Big(1 + A^2 + \cos(\omega \boldsymbol{t})\,[1 + 2A\cos\phi] + 2A\cos\phi\cos(2\omega \boldsymbol{t}) + A^2\cos(3\omega \boldsymbol{t})\Big). \quad (1)$$

Hence, by imprinting an arbitrary phase value on the sidebands and then comparing the experimental temporal intensity profiles

to the analytical ones, we can deduce the relative phase.

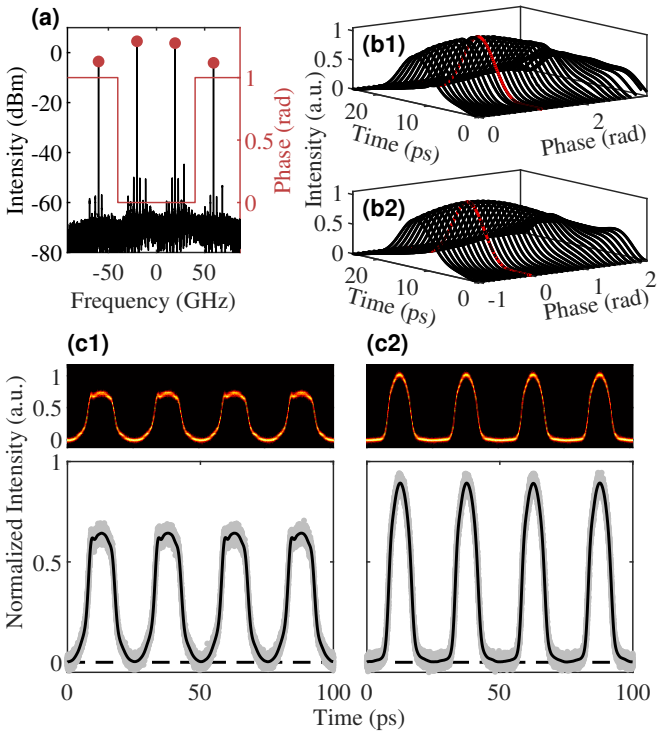

Fig. 3. Experimental measurements. **(a)** Spectral intensity of four central lines used in phase shaping and the imprinted phase profile. **(b)** Experimental temporal intensity profiles after the phase shaping, and the corresponding analytical profiles computed using eq. (1) (panels 1 and 2, respectively). Red line indicates the maximally compressed waveform at 1 rad. **(c)** Initial temporal intensity profile resulting from the full spectrum is compared to the phase-shaped profile where the phase of the higher-order harmonics is compensated by a flat offset of 1 rad (panels 1 and 2, respectively). Raw experimental data are plotted in gray, while black lines depict data filtered with a moving average. False-color plots display measurements in the persistent mode of the OSO. Dashed lines indicate the noise-floor level.

To experimentally implement this principle, we first apply a band-pass filter on the pulse-shaper. This filter selectively preserves the spectral lines within the frequency range −80 to 80 GHz while applying a 40 dB attenuation to the rest of the lines. The measured filtered spectrum is depicted in fig. 3a, from which we determine the ratio between the spectral amplitudes as $A_0 = 0.40$. We then imprint a piecewise-constant symmetrical phase mask, as depicted by the red line in fig. 3a. The size of the intervals is 80 GHz, and the profile is centered on the Stokes lines to exclude the effects of phase-intensity coupling [25]. By gradually varying the imprinted phase on the comb teeth adjacent to the two Stokes lines, and performing repeated measurements of the temporal intensity profile with the OSO, we observe the impact of the phase on the waveforms (fig. 3b). The correspondence between the measurements and the computed analytical waveforms (panel 2 of fig. 3b) using equation eq. (1) with A_0 and the corresponding phase offsets is remarkable. This agreement provides strong validation that the spectral phase is symmetric. When the value of the imprinted phase compensates for the initial phase difference between the Stokes and the adjacent lines, we observe a maximum pulse compression, i.e. maximum peak intensity and shortest duration. This point is highlighted in red in the figure and corresponds to an imprinted phase of 1 rad. This implies that the initial phase difference is $\phi_0 = -1$ rad, which is in very good agreement with the numerical simulation (fig. 2b).

To further investigate the phase features, we measure the intensity profile of the unshaped signal, where no phase compensation is imprinted and all spectral lines are preserved. This gives us the waveform depicted in panel 1 of fig. 3c, which is qualitatively in good agreement with the numerical simulations and has well-pronounced pulses with a duty cycle of 0.42. The differences between the numerical simulations and the experimental measurements can be attributed to the propagation of the pulse train in a few meters of a single-mode fiber in the experimental setup. The generated pulse train is stable and has minimal timing jitter, which is visible in the persistent mode of the measurements depicted in the upper panels of fig. 3c.

We show that with our configuration, which implies stable laser locking, low-noise comb and a relatively simple spectral phase profile, a pulse compression can be achieved with the simplest phase compensation. To do that, we imprint the phase mask, similar to the one depicted in fig. 3a, but now extended to all residual spectral lines, which are no longer attenuated. Although the phase profile is not perfectly compensated for, shaping of the four strongest spectral lines helps significantly enhance the pulse contrast. This allows us to compress the pulses up to a duty cycle of 0.33 and achieve a strong flattening of the pulse floor near zero (panel 2 in fig. 3c). Remarkably, these well-separated pulses exhibit a temporal profile very close to an inverted compact parabola, offering potential advantages in achieving ideal conditions for temporal lenses [26].

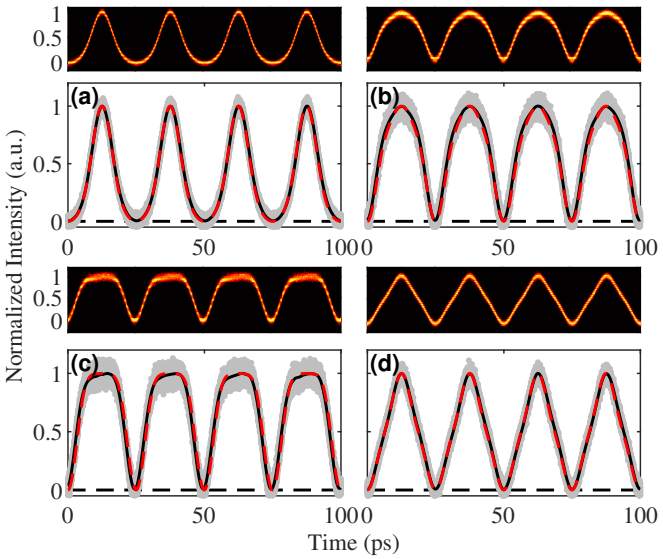

Fig. 4. Experimental results of spectral shaping: **(a)** dark parabolic, **(b)** flat top, **(c)** parabolic and **(d)** triangular waveforms. The dashed red line corresponds to the analytical shape. False color plots display measurements in persistent mode.

Having confirmed the stability of the pulse train and the phase-shaping process, we can now showcase the generation of various other optical waveforms suitable for a variety of applica-

tions [27]. To achieve different intensity profiles, we manipulate the spectral amplitudes and phases of four lines based on the optimal parameters (A, ϕ) described in [24]. Specifically, we target dark parabolic $(0.23, 0.7)$, flat-top $(0.23, 2.24)$, parabolic $(0.24, 1.95)$, and triangular $(0.30, 1.55)$ waveforms [28]. To shape the experimental spectrum, we first cut out all residual lines, as in the first configuration, and then attenuate the two Stokes lines to achieve the required spectral amplitude ratio A. To achieve correct shaping, the initial phase offset $\phi_0 = -1\,\mathrm{rad}$ is systematically subtracted from the parameter ϕ.

The results of the experimental shaping are shown in fig. 4. We observe excellent agreement between the experimental measurements (black lines) and the analytical waveforms (red dashed lines), which are obtained by substituting the given parameters into eq. (1). To estimate a degree of mismatch between the experimentally-measured temporal intensity profile $\boldsymbol{I}_{\mathrm{exp}}(\boldsymbol{t})$ and the theory $\boldsymbol{I}(\boldsymbol{t})$, we use a misfit factor defined as:

$$M^2 = \frac{\int \left[\boldsymbol{I}_{\mathrm{exp}}(\boldsymbol{t}) - \boldsymbol{I}(\boldsymbol{t})\right]^2 dt}{\int \boldsymbol{I}_{\mathrm{exp}}(\boldsymbol{t})^2 dt}. \qquad \textbf{(2)}$$

The obtained values of M for the cases presented in fig. 3 are $0.029, 0.062, 0.049, 0.025$, respectively, which indicates a good quantitative agreement. The measurements were performed in the persistent mode of the OSO, and reveal the excellent stability of our source, with an excellent timing jitter and a low level of intensity noise.

In summary, we used a pulse-shaping method to measure the relative phase between dual-pumped Kerr combs. Our experimental results confirm the symmetric phase relationship between the pump Stokes and adjacent lines, in agreement with numerical simulations. Although our study does not introduce a novel approach, it provides insight into the dual-pumped Kerr comb dynamics and showcases the generation of diverse waveforms. The stability of our low-noise frequency comb underscores its reliability for practical applications.

Our findings suggest potential advantages in dual-pumped Kerr comb applications, emphasizing the absence of abrupt phase differences observed in single continuous-wave pumping. Since compensating the phase shift of all spectral lines is essential to obtain a maximally compressed pulse train, this smoother phase profile can facilitate phase compensation during a compression stage outside the cavity. Research into advanced phase control techniques, such as an iterative optimization loop [8], would complement our setup. This would allow for a comprehensive evaluation of the phase characteristics over a wider spectral range. Future research could explore more complex cavity configurations, media variations, and the influence of environmental factors on waveform stability.

Funding. The authors acknowledge support from the French program 'Investments for the Future' (EIPHI-BFC Graduate School, contract ANR-17-EURE-0002) and the OPTIMAL grant (contract ANR-20-CE30-0004) operated by the French Agence Nationale de la Recherche (ANR), as well as from the Région Bourgogne Franche-Comté and the European Regional Development Fund.

Disclosures. The authors declare no conflicts of interest.

Data availability. Data underlying the results presented in this article are not publicly available at this time, but may be obtained from the authors upon reasonable request.

REFERENCES

1. T. Hänsch, Ann. der Physik **15**, 627 (2006).
2. T. J. Kippenberg, R. Holzwarth, and S. A. Diddams, Science **332**, 555 (2011).
3. T. J. Kippenberg, A. L. Gaeta, M. Lipson, and M. L. Gorodetsky, Science **361**, eaan8083 (2018).
4. S.-W. Huang, J. Yang, S.-H. Yang, M. Yu, D.-L. Kwong, T. Zelevinsky, M. Jarrahi, and C. W. Wong, Phys. Rev. X **7**, 041002 (2017).
5. X. Xue, Y. Xuan, Y. Liu, P.-H. Wang, S. Chen, J. Wang, D. E. Leaird, M. Qi, and A. M. Weiner, Nat. Photonics **9**, 594 (2015).
6. F. Ferdous, H. Miao, D. E. Leaird, K. Srinivasan, J. Wang, L. Chen, L. T. Varghese, and A. M. Weiner, Nat. Photonics **5**, 770 (2011).
7. B. Wang, Z. Yang, S. Sun, and X. Yi, Photonics Res. **10**, 932 (2022).
8. S. B. Papp and S. a. Diddams, Phys. Rev. A **84**, 053833 (2011).
9. I. Coddington, W. C. Swann, and N. R. Newbury, Opt. Lett. **34**, 2153 (2009).
10. F. Cappelli, L. Consolino, G. Campo, I. Galli, D. Mazzotti, A. Campa, M. Siciliani de Cumis, P. Cancio Pastor, R. Eramo, M. Rösch, M. Beck, G. Scalari, J. Faist, P. De Natale, and S. Bartalini, Nat. Photonics **13**, 562 (2019).
11. X. Yi, Q.-F. Yang, K. Y. Yang, and K. Vahala, Nat. Commun. **9**, 3565 (2018).
12. D. C. Cole, E. S. Lamb, P. Del'Haye, S. A. Diddams, and S. B. Papp, Nat. Photonics **11**, 671 (2017).
13. D. Burghoff, Y. Yang, D. J. Hayton, J.-R. Gao, J. L. Reno, and Q. Hu, Opt. Express **23**, 1190 (2015).
14. D. A. Reid, S. G. Murdoch, and L. P. Barry, Opt. Express **18**, 19724 (2010).
15. K. Twayana, F. Lei, Z. Ye, I. Rebolledo-Salgado, Ö. B. Helgason, M. Karlsson, and V. Torres-Company, Opt. Lett. **47**, 3351 (2022).
16. E. Lucas, M. Deroh, and B. Kibler, Laser & Photonics Rev. **17**, 2300041 (2023).
17. G. Huang, E. Lucas, J. Liu, A. S. Raja, G. Lihachev, M. L. Gorodetsky, N. J. Engelsen, and T. J. Kippenberg, Phys. Rev. A **99**, 061801 (2019).
18. S. Coen, M. Tlidi, P. Emplit, and M. Haelterman, Phys. Rev. Lett. **83**, 2328 (1999).
19. P.-H. Wang, J. A. Jaramillo-Villegas, Y. Xuan, X. Xue, C. Bao, D. E. Leaird, M. Qi, and A. M. Weiner, Opt. Express **24**, 10890 (2016).
20. G. Danion, L. Frein, D. Bacquet, G. Pillet, S. Molin, L. Morvan, G. Ducournau, M. Vallet, P. Szriftgiser, and M. Alouini, Opt. Lett. **41**, 2362 (2016).
21. M. Deroh, E. Lucas, and B. Kibler, Opt. Lett. **48**, 6388 (2023).
22. A. M. Clarke, D. G. Williams, M. A. F. Roelens, and B. J. Eggleton, J. Light. Technol. **28**, 97 (2010).
23. Z. Jiang, C.-B. Huang, D. E. Leaird, and A. M. Weiner, J. Opt. Soc. Am. B **24**, 2124 (2007).
24. C. Finot, Opt. Lett. **40**, 1422 (2015).
25. N. Quoc Ngo and Y. Song, Opt. Lett. **36**, 915 (2011).
26. V. Torres-Company, J. Lancis, and P. Andrés, "Space-Time Analogies in Optics," in *Progress in Optics,* , vol. 56 (Elsevier, 2011), pp. 1–80.
27. S. T. Cundiff and A. M. Weiner, Nat. Photonics **4**, 760 (2010).
28. J. Fatome, K. Hammani, B. Kibler, and C. Finot, Laser Phys. Lett. **13**, 015102 (2015).

FULL REFERENCES

1. T. Hänsch, "Einstein Lecture – Passion for precision," Ann. der Physik **15**, 627–652 (2006).
2. T. J. Kippenberg, R. Holzwarth, and S. A. Diddams, "Microresonator-based optical frequency combs." Science **332**, 555–9 (2011).
3. T. J. Kippenberg, A. L. Gaeta, M. Lipson, and M. L. Gorodetsky, "Dissipative Kerr solitons in optical microresonators," Science **361**, eaan8083 (2018).
4. S.-W. Huang, J. Yang, S.-H. Yang, M. Yu, D.-L. Kwong, T. Zelevinsky, M. Jarrahi, and C. W. Wong, "Globally Stable Microresonator Turing Pattern Formation for Coherent High-Power THz Radiation On-Chip," Phys. Rev. X **7**, 041002 (2017).
5. X. Xue, Y. Xuan, Y. Liu, P.-H. Wang, S. Chen, J. Wang, D. E. Leaird, M. Qi, and A. M. Weiner, "Mode-locked dark pulse Kerr combs in normal-dispersion microresonators," Nat. Photonics **9**, 594–600 (2015).
6. F. Ferdous, H. Miao, D. E. Leaird, K. Srinivasan, J. Wang, L. Chen, L. T. Varghese, and A. M. Weiner, "Spectral line-by-line pulse shaping of on-chip microresonator frequency combs," Nat. Photonics **5**, 770–776 (2011).
7. B. Wang, Z. Yang, S. Sun, and X. Yi, "Radio-frequency line-by-line Fourier synthesis based on optical soliton microcombs," Photonics Res. **10**, 932 (2022).
8. S. B. Papp and S. a. Diddams, "Spectral and temporal characterization of a fused-quartz-microresonator optical frequency comb," Phys. Rev. A **84**, 053833 (2011).
9. I. Coddington, W. C. Swann, and N. R. Newbury, "Coherent linear optical sampling at 15 bits of resolution," Opt. Lett. **34**, 2153 (2009).
10. F. Cappelli, L. Consolino, G. Campo, I. Galli, D. Mazzotti, A. Campa, M. Siciliani de Cumis, P. Cancio Pastor, R. Eramo, M. Rösch, M. Beck, G. Scalari, J. Faist, P. De Natale, and S. Bartalini, "Retrieval of phase relation and emission profile of quantum cascade laser frequency combs," Nat. Photonics **13**, 562–568 (2019).
11. X. Yi, Q.-F. Yang, K. Y. Yang, and K. Vahala, "Imaging soliton dynamics in optical microcavities," Nat. Commun. **9**, 3565 (2018).
12. D. C. Cole, E. S. Lamb, P. Del'Haye, S. A. Diddams, and S. B. Papp, "Soliton crystals in Kerr resonators," Nat. Photonics **11**, 671–676 (2017).
13. D. Burghoff, Y. Yang, D. J. Hayton, J.-R. Gao, J. L. Reno, and Q. Hu, "Evaluating the coherence and time-domain profile of quantum cascade laser frequency combs," Opt. Express **23**, 1190 (2015).
14. D. A. Reid, S. G. Murdoch, and L. P. Barry, "Stepped-heterodyne optical complex spectrum analyzer," Opt. Express **18**, 19724 (2010).
15. K. Twayana, F. Lei, Z. Ye, I. Rebolledo-Salgado, Ö. B. Helgason, M. Karlsson, and V. Torres-Company, "Differential phase reconstruction of microcombs," Opt. Lett. **47**, 3351–3354 (2022).
16. E. Lucas, M. Deroh, and B. Kibler, "Dynamic Interplay Between Kerr Combs and Brillouin Lasing in Fiber Cavities," Laser & Photonics Rev. **17**, 2300041 (2023).
17. G. Huang, E. Lucas, J. Liu, A. S. Raja, G. Lihachev, M. L. Gorodetsky, N. J. Engelsen, and T. J. Kippenberg, "Thermorefractive noise in silicon-nitride microresonators," Phys. Rev. A **99**, 061801 (2019).
18. S. Coen, M. Tlidi, P. Emplit, and M. Haelterman, "Convection versus Dispersion in Optical Bistability," Phys. Rev. Lett. **83**, 2328–2331 (1999).
19. P.-H. Wang, J. A. Jaramillo-Villegas, Y. Xuan, X. Xue, C. Bao, D. E. Leaird, M. Qi, and A. M. Weiner, "Intracavity characterization of micro-comb generation in the single-soliton regime," Opt. Express **24**, 10890–10897 (2016).
20. G. Danion, L. Frein, D. Bacquet, G. Pillet, S. Molin, L. Morvan, G. Ducournau, M. Vallet, P. Szriftgiser, and M. Alouini, "Mode-hopping suppression in long Brillouin fiber laser with non-resonant pumping," Opt. Lett. **41**, 2362 (2016).
21. M. Deroh, E. Lucas, and B. Kibler, "Dispersion engineering in a Brillouin fiber laser cavity for Kerr frequency comb formation," Opt. Lett. **48**, 6388 (2023).
22. A. M. Clarke, D. G. Williams, M. A. F. Roelens, and B. J. Eggleton, "Reconfigurable Optical Pulse Generator Employing a Fourier-Domain Programmable Optical Processor," J. Light. Technol. **28**, 97–103 (2010).
23. Z. Jiang, C.-B. Huang, D. E. Leaird, and A. M. Weiner, "Spectral line-by-line pulse shaping for optical arbitrary pulse-train generation," J. Opt. Soc. Am. B **24**, 2124 (2007).
24. C. Finot, "40-GHz photonic waveform generator by linear shaping of four spectral sidebands," Opt. Lett. **40**, 1422 (2015).
25. N. Quoc Ngo and Y. Song, "On the interrelations between an optical differentiator and an optical Hilbert transformer," Opt. Lett. **36**, 915 (2011).
26. V. Torres-Company, J. Lancis, and P. Andrés, "Space-Time Analogies in Optics," in *Progress in Optics,* vol. 56 (Elsevier, 2011), pp. 1–80.
27. S. T. Cundiff and A. M. Weiner, "Optical arbitrary waveform generation," Nat. Photonics **4**, 760–766 (2010).
28. J. Fatome, K. Hammani, B. Kibler, and C. Finot, "80 GHz waveform generated by the optical Fourier synthesis of four spectral sidebands," Laser Phys. Lett. **13**, 015102 (2015).